Inorganic Chemistry

Article

pubs.acs.org/IC

Heteronuclear Ir(III)−Ln(III) Luminescent Complexes: Small-Molecule Probes for Dual Modal Imaging and Oxygen Sensing

Atanu Jana,[†] Bethany J. Crowston,[†] Jonathan R. Shewring,[†] Luke K. McKenzie,[†,‡] Helen E. Bryant,[‡] Stanley W. Botchway,[§] Andrew D. Ward,[§] Angelo J. Amoroso,[⊥] Elizabeth Baggaley,*[,†] and Michael D. Ward*[,†]

[†]Department of Chemistry, University of Sheffield, Sheffield, S3 7HF, United Kingdom

[‡]Department of Oncology & Metabolism, University of Sheffield, Sheffield, S10 2RX, United Kingdom

[§]Rutherford Appleton Laboratory, STFC, Research Complex at Harwell, Harwell Science and Innovation Campus, Didcot, OX11 0FA, United Kingdom

[⊥]School of Chemistry, Cardiff University, Main Building, Park Place, Cardiff CF10 3AT, United Kingdom

Supporting Information

ABSTRACT: Luminescent, mixed metal d−f complexes have the potential to be used for dual (magnetic resonance imaging (MRI) and luminescence) *in vivo* imaging. Here, we present dinuclear and trinuclear d−f complexes, comprising a rigid framework linking a luminescent Ir center to one (**Ir·Ln**) or two (**Ir·Ln$_2$**) lanthanide metal centers (where Ln = Eu(III) and Gd(III), respectively). A range of physical, spectroscopic, and imaging-based properties including relaxivity arising from the Gd(III) units and the occurrence of Ir(III) → Eu(III) photoinduced energy-transfer are presented. The rigidity imposed by the ligand facilitates high relaxivities for the Gd(III) complexes, while the luminescence from the Ir(III) and Eu(III) centers provide luminescence imaging capabilities. Dinuclear (**Ir·Ln**) complexes performed best in cellular studies, exhibiting good solubility in aqueous solutions, low toxicity after 4 and 18 h, respectively, and punctate lysosomal staining. We also demonstrate the first example of oxygen sensing in fixed cells using the dyad **Ir·Gd**, via two-photon phosphorescence lifetime imaging (PLIM).

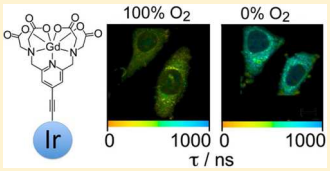

INTRODUCTION

The use of transition-metal luminophores to sensitize luminescence from lanthanide(III) ions in mixed d−f complexes has attracted recent attention from many researchers.[1] The long-lived excited states of many d-block luminophores with triplet excited states make them excellent energy donors whose excited-state energy can be tuned over a wide range by control of ligand type and substituents; in addition, numerous straightforward synthetic methods exist to combine d-block and f-block units such that d−f energy-transfer can occur with the d-block unit acting as the light-harvesting antenna for the lanthanide ion, for which direct f−f excitation is Laporte-forbidden.[1] Among such d−f hybrids the extensive family of cyclometalated phenyl-pyridine/Ir(III) complexes, with their high energy and long-lived triplet excited states that result in blue or green luminescence,[2] have proven to be effective energy-donors for generating luminescence from lanthanides such as Eu(III), Tb(III), Yb(III), and Nd(III) in Ir/Ln dyads.[3,4] The first example came from De Cola and co-workers, who demonstrated that the combination of blue Ir(III)-based emission and red Eu(III)-based emission from a single molecular edifice could be used to generate white light,[4a] and many other examples have been reported since then.

In addition, the use of luminescent transition-metal and lanthanide complexes with long-lived excited states has become very popular in bioimaging applications over the past decade.[5,6] This, combined with technological developments in electronic shutters and optics, has resulted in time-resolved imaging techniques becoming more commonplace in the biosciences. These techniques include the simple rejection of short-lived background autofluorescence via time gating, and "lifetime mapping" using a combination of single photon counting and scanning confocal microcopy, as demonstrated by phosphorescence lifetime imaging (PLIM) and time-resolved emission-imaging microscopy (TREM).[7]

One area that has benefited from these developments is the real-time detection and quantification of oxygen via phosphorescence quenching.[7a,c−f,8] Molecular oxygen has a triplet ground-state configuration and is an effective quencher of the triplet-based phosphorescence displayed by transition-metal complexes. Molecular oxygen also plays a key role in many physiological processes, ATP generation, and mitochondrial function.[9d−f] Low or inadequate levels of oxygen, referred to as hypoxia, are important features in solid tumors, inflammatory diseases, and Alzheimer's disease.[9a−c,g] Hence, the ability to monitor oxygen concentration *in vivo* and *in vitro*, under real-time noninvasive conditions, is extremely desirable for diagnostics and treatment. Optical oxygen monitoring and imaging using lifetime-based techniques have advantages over intensity-based ones. Decay of photoexcited molecules typically follows first-order decay kinetics, so lifetime measurements are

Received: March 21, 2016

DOI: 10.1021/acs.inorgchem.6b00702
Inorg. Chem. XXXX, XXX, XXX−XXX

not affected by the intensity of the excitation light, and lifetime measurements are a property of the individual molecule, and are therefore, largely concentration-independent. Measuring the emission lifetime of a probe, rather than the emission intensity, provides a quantitative, noninvasive method by which intercellular oxygen concentrations can be monitored. Intensity-based measurements can be used for quantitative oxygen sensing with ratiometric probes, where the emissive molecule is both the probe and the internal calibrant. Recent examples of oxygen detection using luminescent transition-metal complexes have involved Pt(II) complexes,[7a,8c−e,10] Pd(II) porphyrins,[8b,11] Ru(II)[12] and Ir(III)[8a,13] complexes, including iridium-based upconverting nanoparticles doped with lanthanides.[13b]

As part of a study to investigate the use of d/f hybrid complexes as cellular imaging probes, we recently reported the preparation and study of complexes **Ir·Eu** and **Ir·Gd** (Figure 1),

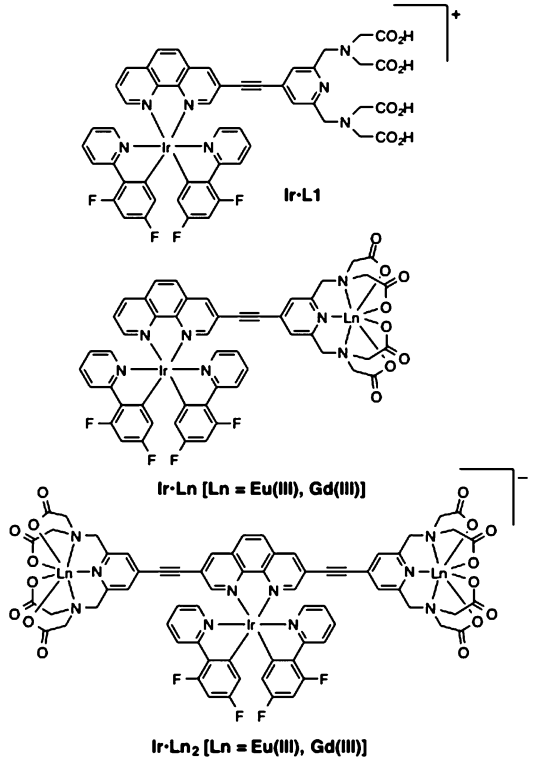

Figure 1. Structures of the dinuclear and trinuclear complexes discussed in this paper, and a mononuclear Ir(III) complex **Ir·L1** used in the DFT calculations.

in which a strongly luminescent $[Ir(F_2ppy)_2(phen)]^+$ unit is connected to a stable lanthanide(III) polyamino-carboxylate chelate via a fully conjugated alkyne bridge.[14] The design of these complexes has three particularly beneficial features. First, the conjugated pathway connecting the two metal centers allows efficient Ir(III) → Eu(III) energy transfer by the Dexter mechanism, which requires electronic coupling between donor and acceptor.[1c,15] Thus, excitation of the Ir(III) unit under either single-photon or two-photon conditions was followed by *partial* Ir(III) → Eu(III) energy transfer to give a mixture of green Ir(III)-based emission (microsecond time scale) and red Eu(III)-based emission (millisecond time scale). Second, the extended conjugated bridge, which is involved in metal-to-ligand charge transfer (MLCT) transitions, may afford a significant two-photon absorption cross section, which will assist with imaging under two-photon excitation conditions. Third, the rigidity imparted to the complex by the rigid rodlike structure resulted in a high relaxivity for the mononuclear Gd(III) center associated with slow tumbling in solution,[16] and we note that d/f complexes combining a luminescent unit and a Gd(III) unit for dual-mode luminescence imaging/magnetic resonance imaging (MRI) have attracted particular interest recently.[17] Generally, for MRI-based applications, the required high relaxivity for protons of water molecules arises from a combination of factors, such as the number of sites available for water to coordinate to the Gd(III) center and their exchange rate (inner-sphere relaxivity), interactions between the Gd(III) center and more-remote water molecules (outer-sphere relaxivity), the rotational correlation time of the molecules in solution, and the longitudinal and transverse electron spin relaxation times of Gd(III), as encapsulated in Solomon−Bloembergen−Morgan theory.[18]

In this follow-up paper, we report on two related areas. First, we have substantially extended the scope of the cellular imaging studies performed with **Ir·Eu** and **Ir·Gd**, demonstrating in particular how we can use the lifetime of the Ir(III)-based luminescence as a probe for the oxygen concentration in cells under *in vitro* conditions. Second, we report the new trinuclear complexes **Ir·Eu$_2$** and **Ir·Gd$_2$** (Figure 1) in which two Ln(III) units are pendant from the central $[Ir(F_2ppy)_2(phen)]^+$ and describe their photophysical properties and use in imaging studies.

RESULTS AND DISCUSSION

Synthesis of New Trinuclear Complexes. Synthesis of the trinuclear **Ir·Ln$_2$** complexes follows the same general methodology as used for the dinuclear **Ir·Ln** complexes that were reported earlier (Scheme 1).[14] The ester-protected pyridine-2,6-bis(imino-diacetate) unit, which ends up as the Ln(III) binding site, contains a central pyridyl group, which can be functionalized with a Br atom at the C^4 position (precursor **A**). This permits its connection to the $[Ir(F_2ppy)_2(phen)]^+$ sensitizer via alkynyl linkages introduced in a Sonogashira coupling reaction. Whereas the use of 3-ethynyl-1,10-phenanthroline afforded the dinuclear **Ir·Ln** complexes using this methodology,[14] in this new work use of 3,8-di(ethynyl)-1,10-phenanthroline (precursor **B**) allowed connection of the Br-functionalized bis(imino-diacetate) unit to both alkynyl sites to give compound **C**. After assembling the component binding sites in this way, coordination of the phenanthroline unit of **C** to an $\{Ir(F_2ppy)_2\}^+$ unit, and unmasking of the amino/carboxylate binding site by removal of the esters, followed by incorporation of Eu(III) or Gd(III), all used standard methods. Incorporation of the pyridyl group into the lanthanide binding site—in contrast to use of the cyclen-tricarboxylate chelate that we used in our earlier work[3f]—allows the Sonogashira coupling to provide a fully conjugated pathway between the Ir(III) and lanthanide (Ln) centers.

Accordingly, these trinuclear complexes **Ir·Ln$_2$** should be expected to have all of the same benefits arising from their structure as do the dinuclear ones, viz, efficient Ir(III) → Eu(III) energy transfer; a two-photon absorption cross section sufficient for imaging purposes; and structural rigidity to impart high relaxivity to the Gd(III) units.

Steady-State and Time-Resolved Luminescence Properties of the Trinuclear Complexes. UV-vis absorption spectral data of the complexes in water are summarized in Table 1. Intense absorptions in the UV region are due to

DOI: 10.1021/acs.inorgchem.6b00702
Inorg. Chem. XXXX, XXX, XXX−XXX

Scheme 1. Procedure for the Synthesis of the Trinuclear Ir·Ln$_2$ Complexes

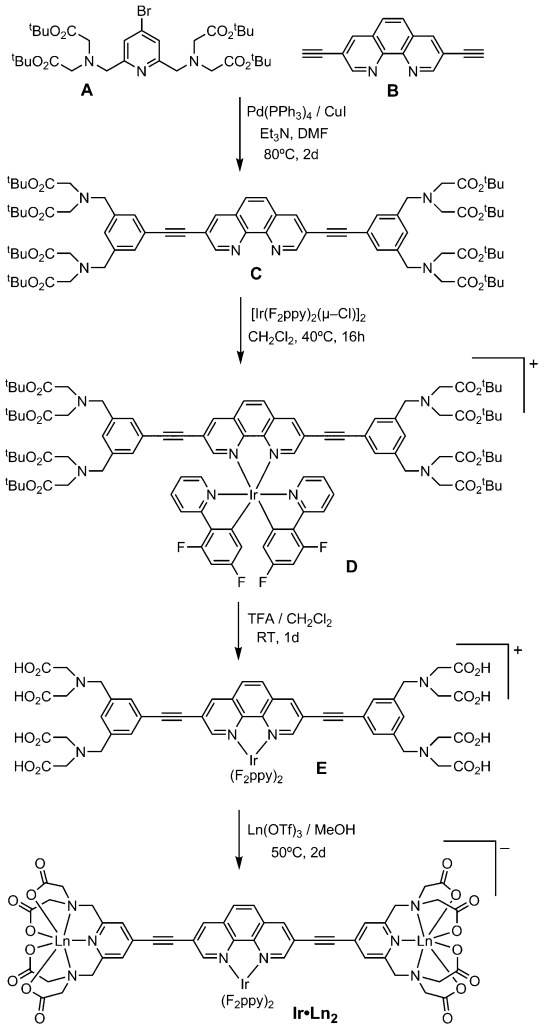

ligand-centered $\pi \rightarrow \pi^*$ electronic transitions; the weak shoulder and long tail between 400 and 550 nm are ascribed to Ir(III) → phen ^{3}MLCT transitions (see Figure S13 in the Supporting Information). It was observed that there is an ∼10−15 nm bathochromic (red) shift, as well as an increase in intensity, of the absorption bands in the case of **Ir·Ln$_2$**, compared to the **Ir·Ln** complexes, which we ascribe to (i) the greater extent of the conjugated network on the substituted phenanthroline ligand in the latter case, and (ii) the presence of two Ln(III) units and their associated aromatic ligands instead of just one.

Luminescence spectra (see Figure 2) of **Ir·Ln** and **Ir·Ln$_2$** were recorded in aerated aqueous solution upon excitation at

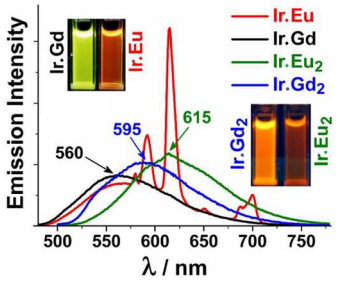

Figure 2. Luminescence spectra of the complexes (10^{-5} M in water). λ_{ex} = 400 nm in each case. Insets show the visual appearance under a UV lamp.

400 nm. In **Ir·Gd$_2$**, the Ir(III)-based luminescence maximum is observed at 595 nm: this is significantly red-shifted, compared to **Ir·Gd** (560 nm), which is a consequence of the more-extended π-network around the phen ligand involved in the MLCT transition, which will stabilize its lowest unoccupied molecular orbital (LUMO). At 77 K (1:4 MeOH/EtOH frozen glass), the rigidochromism expected from a charge-transfer state is clear (see Figure 3), with the highest-energy emission

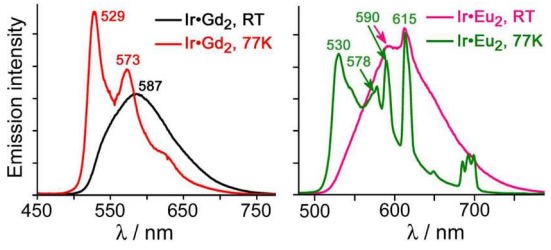

Figure 3. (Left) Luminescence spectra in MeOH/EtOH (1:4) of **Ir·Gd$_2$**, in fluid solution at RT (black) and as a frozen glass at 77 K (red). (Right) Luminescence spectra in MeOH/EtOH (1:4) of **Ir·Eu$_2$** in fluid solution at RT (pink) and as a frozen glass at 77 K (green). λ_{ex} = 400 nm for all cases.

feature now occurring at 529 nm, indicating a ^{3}MLCT energy of 18 900 cm^{-1} (compared to 20 200 cm^{-1} for **Ir·Gd**). Significantly, this energy value for the Ir(III) → phen ^{3}MLCT state is now marginal for efficient sensitization of the emissive $^5D_0$ level of Eu(III), which lies at 17 500 cm^{-1} — the

Table 1. UV-vis Absorption and Luminescence Spectral Data for the Complexes[a]

compound	λ_{max} [nm] (ε [× 10^{-3} M^{-1} cm^{-1}])	λ_{em} [nm]	τ_1^0, τ_2^0 [ns][b]	τ_1, τ_2 [ns][b]	ϕ[c]	ref
Ir·Gd	242 (46), 285 (42), 338 (22)	560	1100, 450	640, 220	0.048	ref 14
Ir·Eu	242 (50), 283 (44), 343 (23)	578, 590, 615, 684, 697[d]	780, 116	510, 95		ref 14
D	241 (81), 285 (79), 355 (52)	552	1470, 275			this work
E	241 (93), 290 (96), 356 (73)	590	890, 150			this work
Ir·Gd$_2$	242 (112), 292 (119), 358 (104)	595	1260, 233		0.026	this work
Ir·Eu$_2$	241 (118), 292 (127), 357 (111)	616[b]	1240, 168			this work

[a]All measurements were carried out in air-equilibrated water at room temperature. The excitation wavelength for luminescence studies was 400 nm in every case. [b]Ir(III)-based luminescence lifetimes: all complexes showed dual-exponential luminescence decay (see main text). τ = air-equilibrated solution. τ^0 = argon-equilibrated solution. [c]Quantum yield values in aerated solvent recorded in DMSO against 1,3-di(2-pyridyl)benzene platinum(II) chloride in CH_2Cl_2 as a reference (φ = 0.039; see ref 20) [d]Eu(III)-based emission maxima, which partly obscure the Ir(III)-based emission; see main text.

DOI: 10.1021/acs.inorgchem.6b00702
Inorg. Chem. XXXX, XXX, XXX−XXX

gradient for energy transfer is only 1400 cm^{-1} — so, on this basis, we might not see efficient sensitization of Eu(III)-based luminescence in **Ir·Eu$_2$**, as a gradient of ca. 2000 cm^{-1} for energy transfer at room temperature (RT) is normally considered necessary to prevent thermally activated back-energy transfer.[3e,19] Quantum yield values of dyad **Ir·Gd** (Φ = 0.048) and triad **Ir·Gd$_2$** (Φ = 0.026) were measured in dimethyl sulfoxide (DMSO), showing that the lower-energy luminescence of **Ir·Gd$_2$** is also slightly lower in intensity.

Comparison of the luminescence spectra of dyad **Ir·Eu** and triad **Ir·Eu$_2$** demonstrate nicely the differing ability of their Ir(III)-centered ^{3}MLCT states to sensitize Eu(III) emission (Figure 2). The luminescence spectrum of **Ir·Eu** in water (reported previously[14]) shows how significant Ir(III) → Eu(III) EnT (energy transfer) has occurred, with the Ir(III)-based luminescence reduced in intensity, compared to what was observed for **Ir·Gd** and the characteristic sharp emission lines from Eu(III) superimposed on the low-energy tail of the broad Ir(III)-based luminescence. In contrast, in the luminescence spectrum of **Ir·Eu$_2$** (Figure 2, green trace) the sharp Eu(III)-based emission lines are barely visible. They are clearly present to some extent as they distort the envelope of the Ir(III)-based luminescence: a small just-visible feature at 615 nm may be ascribed to the tip of the most intense Eu(III)-emission component, but the sensitized Eu(III)-based luminescence is clearly very much weaker in **Ir·Eu$_2$** than in **Ir·Eu**. Quantum yield determinations for dyad **Ir·Eu** and triad **Ir·Eu$_2$** were not performed, because of substantial overlap of the Ir(III)-based Eu(III)-based emission components; and, in any case, a single quantum yield value encapsulating the combined emission from two quite different luminophores is not a useful parameter.

The differences in Ir(III) → Eu(III) EnT between **Ir·Eu** and **Ir·Eu$_2$** are also apparent from time-resolved measurements. **Ir·Eu** showed substantial quenching of the Ir(III)-based emission lifetime compared to **Ir·Gd**, associated with an Ir(III) → Eu(III) EnT rate of ca. 6×10^6 s^{-1},[14] there is much less difference between the unquenched Ir(III)-based emission lifetimes of **Ir·Gd$_2$** (τ = 1260 and 230 ns) and **Ir·Eu$_2$** (τ = 1240 and 168 ns). Based on the shorter-lived emission component, we can estimate an Ir(III) → Eu(III) EnT rate of ca. 1.6×10^6 s^{-1} in **Ir·Eu$_2$**: this comes from eq 1, in which τ_u is the "unquenched" lifetime (i.e., in the Ir/Gd complex) and τ_q is the "quenched" lifetime (i.e., in the Ir/Eu complex).

$$k_{EnT} = \frac{1}{\tau_q} - \frac{1}{\tau_u} \quad (1)$$

The energy-transfer rate constant for **Ir·Eu$_2$** is clearly considerably smaller than that for **Ir·Eu**, because of the smaller thermodynamic gradient, and this is also in agreement with the appearance of the steady-state spectra.

Theoretical Calculations. Quantum mechanical calculations were carried out in an effort to understand the optical properties and charge transfer behavior of the two major Ir(III)-containing rigid skeletons. Calculations were performed on mononuclear Ir(III) complexes **Ir·L1** (Figure 1) and **E** (Scheme 1), i.e., the fully functionalized and deprotected Ir(III) complexes, with the pendant pyridyl/amine/acid binding sites but without the attached Ln(III) ions. All calculations were performed using the Gaussian 09 program suite[21] with Becke's three-parameter hybrid exchange functional (B3LYP);[22] a basis set of 6-31G* was employed for H, C, N, and O atoms and, for Ir(III), we used the LanL2DZ[23] basis set. The calculations revealed that the conjugated phenanthroline-based ligands with alkyne substituents in both **Ir·L1** and **E** are planar. Moreover, there is a prominent (0.149 eV) reduction of energy gap (ΔE) between the highest occupied molecular orbital (HOMO) and LUMO upon moving from **Ir·L1** (ΔE = 2.630 eV) to **E** (ΔE = 2.481 eV; cf. Figures S24 and S25, respectively, in the Supporting Information), which is attributed to the stabilization of the LUMO that results from an effective expansion of the π-electron cloud throughout the rigid rod ligand, with the second alkynyl/pyridine substituent. This finding is fully in agreement with the observed red shift of the absorption bands in **E**, which are in the UV region, characteristic of the $\pi \rightarrow \pi^*$ electronic transition (see Figure S13).

The systems were then carefully analyzed in accord with a number of molecular orbital digrams from HOMO−20 to LUMO+20 to explain other electronic features. In the case of **Ir·L1**, HOMO−2 is mainly concentrated on Ir(III)-based antenna group and the LUMO is located throughout the conjugated fragments (Figure S24). On this basis, we assign the ^{3}MLCT band, observed in the visible region for **Ir·L1**, to be due to the HOMO−2 → LUMO electronic transition (see Figure S26 in the Supporting Information). In the case of the larger complex **E**, HOMO−4 and HOMO−16 have substantial Ir(III)-based character and the LUMO is centered mainly on the extended phen/alkyene ligand, extending to include the pyridyl rings (Figure S25). Thus, the ^{3}MLCT transition could be assigned due to the HOMO−4 → LUMO and HOMO−16 → LUMO electronic transitions (Figure S27 in the Supporting Information).

Time-dependent density functional theory (TD-DFT) (B3LYP/6-31G*) simulations of the electronic spectra of **Ir·L1** and **E** were also performed. The TD-DFT stick spectra obtained from this analysis are in good agreement with the experimental spectra (cf. Figure S26 and S27, and Tables S2−S4 in the Supporting Information). In fact, the ^{3}MLCT-based transitions involving the Ir(III)-dominated MOs are seen to give rise to very weak bands observed in the visible region of the experimentally determined steady-state absorption spectra (cf. Tables S2 and S3).

Relaxivity of Ir·Gd and Ir·Gd$_2$. We reported previously that dinuclear **Ir·Gd** has a relaxivity of 11.9 mM^{-1} s^{-1} in aqueous solution at 37 °C and 20 MHz, which is a value that is considerably higher than that normally observed for mononuclear Gd(III) chelates of this type, which was ascribed to the rigidity of the rod-shaped complex.[14] Trinuclear **Ir·Gd$_2$** is not sufficiently soluble for relaxivity measurements in pure water as solubilities of the order of millimolar (mM) are required. Instead, the relaxivity of **Ir·Gd$_2$** was measured in a DMSO/water (5:95, v/v) mixture, and the relaxivity of **Ir·Gd** was remeasured under the same conditions for comparison, because the presence of DMSO increases solvent viscosity. Note that the relaxivity values for the analogous compounds **Ir·Eu** and **Ir·Eu$_2$** were not measured, since the nonsymmetrical electron configuration of Eu(III) is well-known to result in a spin relaxation time that is too short to alter the relaxivity of protons.[24]

Complex **Ir·Gd**, in this solvent mixture, has a relaxivity slightly higher than in aqueous solution (14.0 mM^{-1} s^{-1}, cf. 11.9 mM^{-1} s^{-1} in water, both at 20 MHz, 37 °C). The relaxivity of **Ir·Gd$_2$** is slightly *lower* than that of **Ir·Gd** (12.6 mM^{-1} s^{-1}) at this frequency, despite the presence of a second Gd(III) center. The relaxivity values of these species are comparable to those of complexes with very similar Gd(III) coordination environments

DOI: 10.1021/acs.inorgchem.6b00702
Inorg. Chem. XXXX, XXX, XXX−XXX

in aqueous solution,[25] but significantly higher (in the case of **Ir·Gd**) than those observed with diethylenetriamine-pentaacetic acid (DTPA) and 1,4,7,10-tetraazacyclododecane-1,4,7,10-tetraacetic acid (DOTA)-like molecules, which are typically 4−5 mM^{-1} s^{-1}. This is mostly due to the rigidity of the local ligand framework about the metal center, leading to fast water exchange rates.[25a] The lower relaxivity of **Ir·Gd$_2$** than **Ir·Gd** at 20 MHz may arise from the complex relationship between rotational correlation time, relaxivity, and measurement frequency:[26] but also, in part, it may arise from the poor solubility of **Ir·Gd$_2$**, which would cause aggregation of the complex and change the effective hydration state of the Gd(III) center.

Imaging Studies Using Ir·Eu and Ir·Gd. During the initial imaging studies with dyads **Ir·Eu** and **Ir·Gd**, we observed that **Ir·Gd** was taken up by MCF7 cells considerably more effectively than **Ir·Eu**,[14] which was a surprise, given their structural similarity: this might be related to a change in coordination number between Eu(III) and Gd(III). Two-photon PLIM measurements confirmed that the differences in Ir(III)-based emission lifetimes, arising from partial quenching by Ir(III) → Eu(III) EnT in **Ir·Eu**, but not in **Ir·Gd**, could also be detected in cells.

Here, we report additional imaging studies using these complexes in HeLa cells. As with MCF7 cells, we noticed that cellular uptake of the two dyads was markedly different. The luminescence intensity observed after 18 h of incubation with **Ir·Gd** was much higher than that observed with **Ir·Eu**, implying a more efficient uptake of **Ir·Gd**. This is apparent in the distance versus luminescence intensity line profiles for the two complexes, following incubation at 100 μM (Figure 4): across

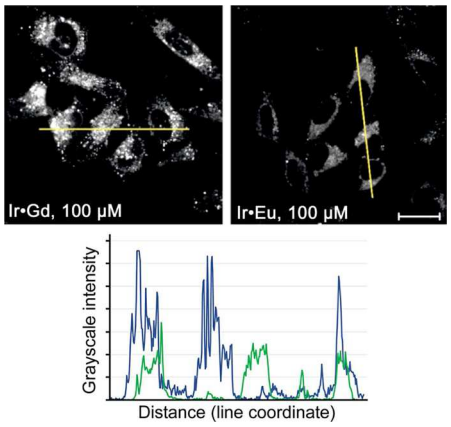

Figure 4. (Top) Comparison of confocal microscopy images taken from HeLa cells treated with **Ir·Gd** and **Ir·Eu** at 100 μM (scale bar = 20 μm). (Bottom) Intensity versus distance plots for **Ir·Gd** (blue) and **Ir·Eu** (green) showing difference in cellular luminescence intensities along the lines shown in the top images. Imaging parameters, optimized for **Ir·Eu** at 100 μM, remained constant for direct comparison. λ_{ex} = 405 nm. λ_{em} = 500−530 nm.

individual cells, **Ir·Gd** displays intensity values that are approximately double that of **Ir·Eu**, with the brightest pixels for the punctate emission showing almost triple the luminescence intensity that was obtained with **Ir·Eu**. If there were no difference in uptake between the two complexes, we would expect to see only a ca. 20% enhancement in emission intensity from **Ir·Eu** to **Ir·Gd** (based on the differences in Ir(III)-based emission intensity between the two complexes arising from partial quenching in **Ir·Eu**). We tentatively attribute this to difference in cellular uptake with a subtle difference in the coordination sphere around the lanthanide ion, as other attributes of the dyads, overall size, charge and lipophilicity are virtually the same. Figure S15 in the Supporting Information shows the comparative uptake of **Ir·Eu** and **Ir·Gd** in HeLa cells across a range of concentrations (100−25 μM), with images being recorded using the same instrument parameters (initially optimized for **Ir·Eu** at 100 μM) to allow direct comparison. Optimizing imaging parameters per sample (Figure S16 in the Supporting Information) allowed the staining pattern of the dyads in HeLa cells to be clearly observed. The staining of **Ir·Eu** and **Ir·Gd** in HeLa cells is very similar to that observed in MCF7 cells, in that emission from the dyads is observed in the cell cytosol with some additional punctate staining. The complexes were not observed to cross the nuclear membrane.

Co-localization studies with lysotracker Red (Figure 5) show a very good correlation with the punctate staining observed for the dyads. Qualitative overlay images (Figure 5, right panel, gray scale), generated using the co-localization threshold in ImageJ, show a good correlation between the punctate Ir(III)-based emission (green) and lysotracker emission (red). Control images (lysotracker only, Figure S17 in the Supporting Information) confirm that there is no crosstalk of lysotracker emission under 405 nm excitation.

The degree of co-localization between lysotracker and the **Ir·Ln** complexes is reflected in the Manders coefficients[27] (obtained using Coloc2 plugin, ImageJ): These are values between 0 and 1, which measure the extent of co-occurrence between red and green pixels (where 0 is no co-occurrence and 1 is perfect co-occurrence). The coefficient M1 takes into account the red channel first, asking the question, "if there is a red pixel, is there also a co-localized green one?" The coefficient M2 is calculated using the green channel first (i.e., "if there is a green pixel, is there also a colocalized red one?").

The M1/M2 values for lysotracker with either **Ir·Eu** or **Ir·Gd** are similar at 0.99/0.73 (lysotracker + **Ir·Eu**) and 0.91/0.87 (lysotracker + **Ir·Gd**). The fact that M1 is close to 1 and M2 is not 0 in both cases indicates that (i) there is a good co-localization between lysotracker and **Ir·Ln**, and (ii) the **Ir·Ln** complexes do not exclusively stain the lysosome, which supports what we see in the steady-state confocal images.

MTT (3-(4,5-dimethylthiazol-2-yl)-2,5-diphenyltetrazolium bromide) toxicity assays show a decrease of ca. 20% in cell survival, particularly at higher incubation concentrations (100 μM) and incubation times (up to 18 h), associated with uptake of the complexes into the cells. However, the reduction in cell viability with the **Ir·Ln** complexes is much less significant with an incubation time of only 4 h: under these conditions, cell survival fractions here are similar to the control experiments. Overall, the dinuclear **Ir·Ln** complexes appear to be only slightly toxic to HeLa cells, even at high concentrations and long incubation times, and under conditions used for imaging and oxygen sensing (see below), these dinuclear complexes do not appear to have any significant effect on cell viability.

Imaging Studies Using Ir·Eu$_2$ and Ir·Gd$_2$. The trinuclear complexes **Ir·Eu$_2$** and **Ir·Gd$_2$** display a very similar staining pattern in HeLa cells to that of the dinuclear complexes (Figure 6). However, their uptake into HeLa cells was observed to be generally poorer than **Ir·Ln** complexes. As size and charge have transpired to be two key factors in cellular uptake of metal-based imaging agents, where small cationic complexes have a

DOI: 10.1021/acs.inorgchem.6b00702
Inorg. Chem. XXXX, XXX, XXX−XXX

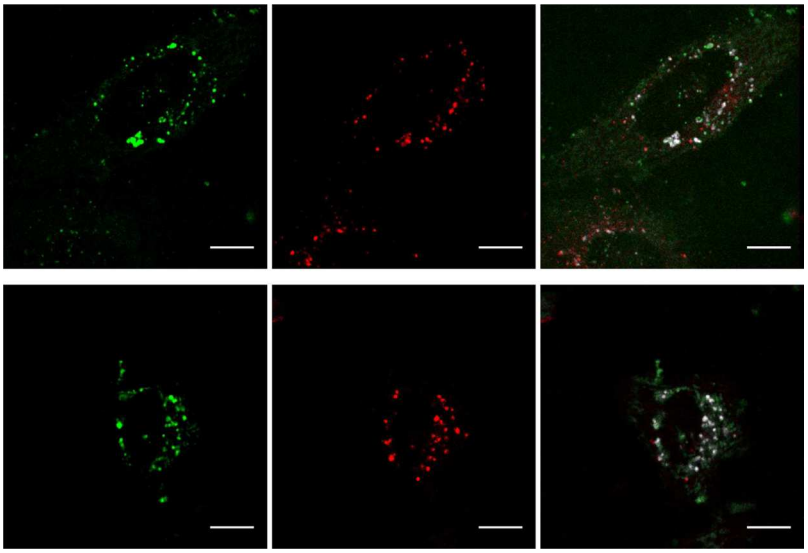

Figure 5. Co-staining of HeLa cells with **Ir·Ln** and lysotracker Red. (Top) **Ir·Eu** and (bottom) **Ir·Gd**. Live HeLa cells were incubated with **Ir·Eu** at 100 μM and **Ir·Gd** at 50 μM in full media for 18 h before the addition of lysotracker Red. Live cells were washed with PBS and imaged in full (phenol-red free) media. (Left) **Ir·Ln**, with λ_{ex}: 405 nm, λ_{em} = 500−550 nm; (middle) lysotracker Red, with λ_{ex} = 561 nm, λ_{em} = 590−700 nm; (right) overlay, with co-localization depicted by gray. (Scale bar = 10 μm throughout.)

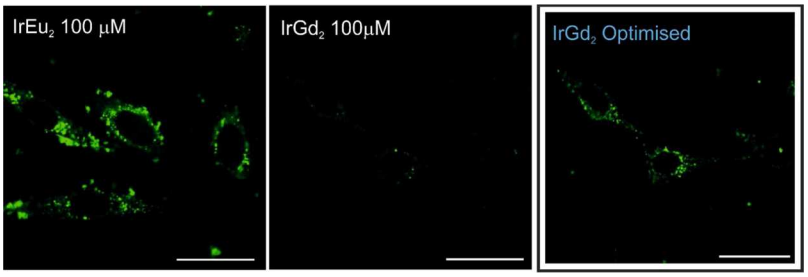

Figure 6. (Left) Comparison of **Ir·Eu$_2$** uptake in live HeLa cells and (middle) **Ir·Gd$_2$** uptake in live HeLa cells. Cells were incubated with **Ir·Ln$_2$** at 100 μM in full media for 18 h, followed by washing and fixation. Imaging parameters (optimized for **Ir·Eu$_2$** at 100 μM) remained constant for both compounds. (Right) **Ir·Gd$_2$** imaged with optimized parameters for this sample. λ_{ex} = 405 nm, λ_{em} = 500−530 nm. (Scale bar = 20 μm throughout.)

tendency to perform the best,[28] it is therefore logical that the larger, anionic triads (**Ir·Ln$_2$**) are less efficiently taken up into mammalian cells than the smaller, neutral dyads (**Ir·Ln**). The uptake trend between the two triad complexes appeared to exhibit behavior opposite to that of the dinuclear complexes, in that **Ir·Eu$_2$** was taken up more effectively than **Ir·Gd$_2$**. Again, such a difference is unexpected, given the structural similarity of the triads, and may arise from a change in coordination number between Eu(III) and Gd(III). However, the mediocre solubility of the triads in aqueous solution, when diluted from a DMSO stock, means that this difference between uptake of **Ir·Eu$_2$** and **Ir·Gd$_2$** may actually be related to solubility. Confocal images of HeLa cells stained with **Ir·Ln$_2$** (Figure 6, left and middle), obtained using an identical set of parameters (initially optimized for **Ir·Eu$_2$** at 100 μM) depict the strong difference between uptake of **Ir·Eu$_2$** and **Ir·Gd$_2$**: the emission intensity arising from the cells stained with **Ir·Eu$_2$** is clearly the brighter of the two, despite the inherently weaker emission of the Ir unit [arising from slight quenching by the Eu(III) ions].

Poor cellular uptake of the trinuclear complexes is reflected in the MTT toxicity data (see Figure S19 in the Supporting Information). The survival fractions of HeLa cells after incubation with 100 μM of either of the trinuclear complexes for 18 h are very similar to those obtained for 0.5% DMSO and 1% DMSO control experiments, implying that uptake into the cells is poor. The relatively poor solubility of the **Ir·Ln$_2$** trinuclear complexes (in comparison to the dinuclear **Ir·Ln** analogues) may contribute to this. Nonetheless, luminescence spectra recorded directly from live HeLa cells (Figure 7) do show that the complexes remain intact during transport across the cell membrane (compare the spectra in Figure 7 with the spectra shown in Figure 2).

O_2 Sensing Using Ir·Gd. The **Ir·Gd** dyad is an ideal candidate for further investigations in time-resolved imaging applications, for many reasons:

(i) it is highly soluble in aqueous solution;
(ii) it can be taken up efficiently into both MCF7 and HeLa cells;
(iii) it exhibits low toxicity;
(iv) it shows appreciable excitation under two-photon excitation; and
(v) it has a luminescence lifetime on the order of hundreds of nanoseconds, which makes lifetime variations easy to measure.

Therefore, we wished to evaluate its suitability for luminescence-based O_2 sensing in cells. To do this, we investigated the emission lifetime of **Ir·Gd** under increasing concentrations of O_2 (using O_2:N_2 mixtures) in aqueous solution, in full cell

DOI: 10.1021/acs.inorgchem.6b00702
Inorg. Chem. XXXX, XXX, XXX−XXX

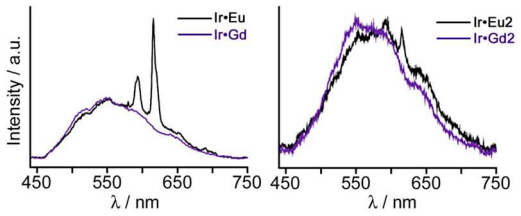

Figure 7. Emission spectra recorded from live HeLa cells after incubation with (left) dinuclear **Ir•Ln** complexes and (right) trinuclear **Ir•Ln$_2$** complexes.

media, using single-photon PLIM, and in fixed HeLa cells, using two-photon PLIM.

Solution measurements (in water and cell media) were recorded by scanning a small area of the bulk solution (inside a MatTek 35 mm glass-bottomed dish), using a 256 × 256 pixel array on an inverted Nikon Ti-E microscope with single photon PLIM imaging capabilities. The entire (homogeneous) 256 × 256 pixel array was analyzed as a single region of interest (ROI) for each oxygen concentration. Superimposed decay traces (Figure S20 in the Supporting Information) clearly show the change in **Ir•Gd** emission lifetime with the changing concentration of O_2. For both solutions, decay curves were best fit to a double exponential model; the major lifetime component (τ_1) matches those recorded in a conventional spectroscopy cuvette, using a lifetime spectrometer.

Lifetime mapping of fixed HeLa cells labeled with **Ir•Gd**, using two-photon PLIM, reveals a distribution of lifetimes across a single cell under air-equilibrated conditions. The higher intensity emission emanating from the punctate staining of the cell lysosomes exhibits a shorter emission lifetime, compared to that of the more-diffuse cytoplasmic staining (Figures 8 and 9). Figure 8 highlights the two different staining patterns as ROI-1 (cytoplasm) and ROI-2 (lysosomes) on a typical two-photon PLIM intensity-based image (where all emitted photons are binned into one channel). Overlaid decay traces (Figure 8c) and distribution histograms (Figure 8a, depicting the distribution of the major component τ_1, after fitting all pixels

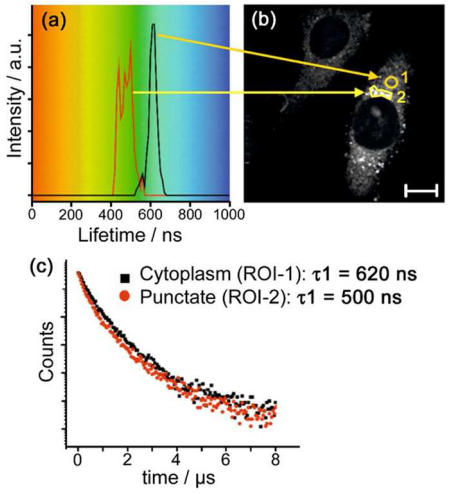

Figure 8. Lifetime distribution of **Ir•Gd** across a single HeLa cell: (a) histogram showing distribution of τ_1 values from ROI-1 (cytoplasm) and ROI-2 (punctate staining), (b) intensity images of fixed HeLa cells stained with **Ir•Gd** (50 μM, 18 h) in air, and (c) decay traces corresponding to ROI 1 (black) and 2 (red). (Scale bar = 10 μm.)

to a double exponential model) from each ROI (see Figure 8b) shows the difference in emission lifetime between cellular locations: for ROI 1, τ_1 = ca. 620 ns; for ROI 2, τ_1 = ca. 500 ns. This variation in lifetime is tentatively attributed to the different local environments experienced by the complex, i.e., acidic cell lysosomes, in comparison to diffuse cytoplasm, rather than concentration of **Ir•Gd** within the cell. In solution, the emission lifetimes of **Ir•Gd** remain constant with concentration across ca. 2 orders of magnitude (1.0×10^{-6} M to 1.0×10^{-4} M, Figure S22 in the Supporting Information). Lifetimes recorded in aqueous solution have a larger percentage contribution from the shorter lifetime component ($\tau_2 \approx 60\%$), in comparison to CH_2Cl_2 solutions ($\tau_2 > 10\%$); however, this contribution decreases to ca. 40% with increasing concentration. The cellular environment is more complex than that of a homogeneous solution and the local concentration of **Ir•Gd** within the lysosomes may be higher than that measured in solution. Therefore, it is possible that aggregation and self-quenching (as is observed in solution for these types of complex)[3b,d,14] also plays a part in the shorter emission lifetime observed at the lysosomes.

Having established the range of luminescence lifetimes within a cell under air, we then repeated the experiment under different concentrations of O_2. Two-photon PLIM imaging of **Ir•Gd** in fixed HeLa cells across a range of O_2 concentrations (Figure 9) shows that (i) the Ir(III)-based emission lifetime is

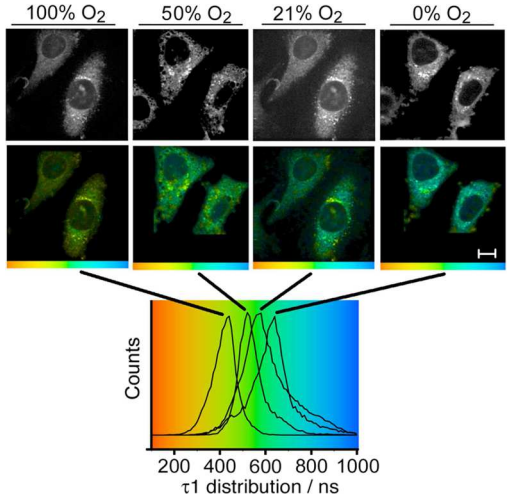

Figure 9. Two-photon PLIM (λ_{ex} = 760 nm) imaging of **Ir•Gd** stained HeLa cells (50 μm, 18 h, fixed) under varying concentrations of O_2. Scale bar = 10 μm.

sensitive to changing levels of O_2, even when fixed inside a complex cell environment, and (ii) the distribution of lifetimes across a single cell is maintained. Four lifetime maps are shown in Figure 9, plotted on the same color scale with the variation from red to blue as the lifetime varies across the range of 0–1000 ns. Within Figure 9, the τ_1 distribution plots change visually from principally orange to principally blue, showing how the luminescence lifetime increases as the O_2 concentration decreases. The range of τ_1 values within each image are also plotted as histograms (below) on the same scale, depicting the change in average luminescence lifetime in a cell with decreasing levels of O_2: average lifetime values of 435, 520, 586, and 644 ns are obtained with relative O_2 concentrations of 100%, 50%, 21%, and 0%, respectively. The response of specific

DOI: 10.1021/acs.inorgchem.6b00702
Inorg. Chem. XXXX, XXX, XXX−XXX

lysosomal and cytoplasmic ROI values with changing O_2 levels are shown in Figure 10.

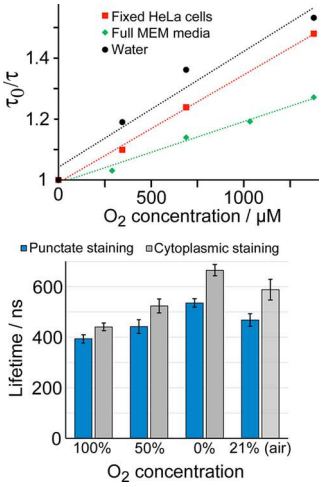

Figure 10. (Top) Stern–Volmer plots of **Ir·Gd** under different oxygen concentrations in fixed HeLa cells (red, $K_{sv} = 3.54 \times 10^{-4}$ μM^{-1}, τ_1 cell average); full cell media (green, $K_{sv} = 2.02 \times 10^{-4}$ μM^{-1}); and water (black, $K_{sv} = 3.80 \times 10^{-4}$ μM^{-1}). (Bottom) Histogram showing **Ir·Gd** lifetime variation across fixed cell. Diffuse cytoplasmic lifetimes (gray) are consistently longer than punctate staining (blue) under varying concentrations of oxygen.

The sensitivity of **Ir·Gd** luminescence lifetime to changing levels of oxygen across the three conditions (fixed cells, water, and full cell media) was quantified using the Stern–Volmer equation (eq 2).

$$\frac{\tau_0}{\tau} = 1 + K_{SV}\cdot[O_2] \quad (2)$$

Quenching constants (K_{sv}) determined from a straight line plot of $[O_2]$ (μM) against τ_0/τ, Figure 10 (where τ_0 is the emission lifetime at 100% N_2), were very similar for fixed HeLa cells and water (3.54×10^{-4} μM^{-1} and 3.80×10^{-4} μM^{-1}, respectively) but slightly lower for full cell media (2.02×10^{-4} μM^{-1}), which indicates some environment-dependent sensitivity of the luminescence toward O_2.

Luminescence lifetime values in full media were observed to be slightly longer than those obtained from aqueous solution or in fixed cells. We believe the longer observed lifetime—and lower sensitivity toward quenching by O_2—in full Modified Eagle's Medium (MEM) cell media is due to the dyad being in a more protected environment when a large protein such as fetal calf serum is present in the bulk solution. Binding to large protein molecules is known to protect small molecules from collisional quenching with dissolved oxygen; protein titrations with a luminescent Ru(II) complex have shown that emission intensity and lifetime increases as the concentration of protein increases.[29] Although proteins and subcellular structures also exist in fixed cells, the region of interest (in this case, the entire cell) is nonhomogenous; meaning the lifetime observed from a single cell is a summative average of the emission properties of **Ir·Gd** from multipule cellular environments (potentially at different concentrations). The more homogeneous nature of MEM in cell media solution provides a more uniformly protected environment for **Ir·Gd**, which, when compared to an entire cell, exhibits a longer lifetime.

For a complex to be a suitable biological O_2 sensor, a significant difference in emission lifetime is required across physiological concentrations of O_2, typically 1%–11%.[30] Platinum and palladium porphyrin-based systems, which have received much attention as oxygen sensors in recent years, typically show a 2-fold reduction in emission lifetime (τ_{air} = 60–70 μs) as the proportion of O_2 increases from 0 to 21%.[7e,10b–d] Although the O_2 sensitivity of **Ir·Gd** is lower than such porphyrin systems, this small molecule design does have some advantages; synthetically, they are less time-consuming (fewer synthetic steps than large porphyrins), the Gd center potentially enables this single molecule to act as an MRI probe in addition to a luminescence-based probe, and the luminescence lifetime (>10 μs) allows for faster data collection using point scanning, time-resolved techniques. The fact that a clear difference in luminescence lifetime is observed in fixed HeLa cells with **Ir·Gd** and changing $[O_2]$ is promising for a dynamic live cell model. Furthermore, modification of the Ir(III) chromophore to elongate the τ^0 Ir(III) lifetime (closer to ca. 5 μs rather than ca. 1 μs) would contribute toward improved O_2 sensitivity, as is observed with other Ir(III)-containing oxygen sensors.[13b,d]

CONCLUSIONS

In conclusion, dinuclear and trinuclear **Ir·Ln** and **Ir·Ln$_2$** complexes, in which a phosphorescent Ir(III)-based unit is connected to one or two water-stable lanthanide/amino-carboxylate units via a rigid, conjugated bridging connection, have been prepared. The dinuclear complexes performed better than their trinuclear counterparts for luminescence cell imaging and also in terms of relaxivity (for Gd complexes). For dual (luminescence + MRI) imaging applications, the complex **Ir·Gd** is a promising candidate. With excellent luminescence imaging capabilities and low toxicity, it also displays unusually high relaxivity for a small molecule containing just one Gd(III) center. Variations in luminescence lifetime allow it to be used as a sensor toward molecular oxygen, an important biological analyte, in solution and *in vitro*. However, to be considered an ideal *in vivo* sensor for O_2, a more significant change in the phosphorescence lifetime across physiological O_2 concentrations would be required: achieving this in future generations is well within the scope of well-understood synthetic modifications to the Ir(III)-complex core. Thus, this complex provides an excellent platform to optimize a dual-imaging oxygen-sensitive probe.

EXPERIMENTAL SECTION

Syntheses. *Compound* **C**. The mechanism used to form ligand **C** is shown in Scheme 1. Precursors **A** (1.48 g, 2.2 mmol) and **B** (0.228 g, 1.0 mmol) (see Scheme 1) were dissolved in anhydrous DMF (20 cm^3) under argon. $Pd(PPh_3)_4$ (92 mg, 0.08 mmol) and CuI (67 mg, 0.35 mmol) were placed in a separate 100 cm^3 Schlenk tube, which was evacuated and backfilled with argon several times. The solution of **A** and **B** was transferred into this reaction vessel via a clean and dry cannula. Finally, anhydrous triethylamine (5 cm^3) was added to the reaction mixture, which was kept at 80 °C for 3 days with constant stirring. After removal of the solvent under reduced pressure, the deep brown residue was dissolved in dichloromethane (DCM, 150 cm^3), then washed with aqueous potassium cyanide (2%, 70 cm^3) and with water (2 × 200 cm^3). The organic layer was dried over $MgSO_4$ and purified by column chromatography on alumina, eluting initially with CH_2Cl_2 and then with 1% MeOH in CH_2Cl_2, to furnish **C** as an orange semisolid (1.16 g, 82%). ***Caution: Potassium cyanide (KCN) is highly toxic; it can prevent cellular respiration and should be handled***

DOI: 10.1021/acs.inorgchem.6b00702
Inorg. Chem. XXXX, XXX, XXX–XXX

with care. Extra training may be required by the user. ^{1}H NMR (500 MHz, $CDCl_3$, 298 K, TMS): δ 1.49 (s, 72H), 3.55 (s, 16H), 4.10 (s, 8H), 7.53, (bs, 4H), 7.76 (bs, 2H), 7.92 (bs, 2H), 8.45 (bs, 2H). ^{13}C NMR (125 MHz, $CDCl_3$, 298 K, TMS): δ = 28.2, 56.1, 59.5, 81.3, 92.0, 122.9, 127.2, 128.5, 129.7, 131.9, 132.2, 133.0, 133.4, 133.8, 138.5, 152.2, 160.1, 170.3. ESI-MS: m/z 1411.8 [20%, $(M + H)^+$]; 706.4 [100%, $(M + 2H)^{2+}$].

*[Ir(dfppy)$_2$(**C**)]PF$_6$ (Complex **D**).* A suspension of **C** (0.706 g, 0.5 mmol) and $[\{Ir(dfppy)_2Cl\}_2]$ (0.304 g, 0.25 mmol) in dry CH_2Cl_2/MeOH (50 cm^3, 4:1 v/v) was kept at reflux for 16 h under an inert atmosphere. After cooling the reaction mixture to RT, ca. 15 equiv of NH_4PF_6 (1.22 g, 7.5 mmol) was added to the reaction mixture with stirring. After 6 h, the reaction mixture was evaporated near to dryness and 5 cm^3 of CH_2Cl_2 was added to the residue to completely dissolve the organic substances. Residual NH_4PF_6 was filtered off and the dark solution was concentrated. The crude product was purified by column chromatography on alumina, eluting initially with CH_2Cl_2 and then with 2% MeOH in CH_2Cl_2, to furnish complex **D** as a deep yellow crystalline material (0.724 g, 70%). ^{1}H NMR (400 MHz, $CDCl_3$, 298 K, TMS): δ 1.47 (s, 72H), 3.50 (s, 16H), 4.05 (s, 8H), 5.76 (dd, 1H), 5.78 (dd, 1H), 6.62−6.67 (m, 2H), 7.08−7.10 (m, 2H), 7.25 (s, 1H), 7.41−7.43 (m, 2H), 7.63 (s, 1H), 7.70 (s, 2H), 7.81−7.85 (m, 2H), 8.25−8.33 (m, 4H), 8.37−8.39 (m, 2H), 8.76 (d, 1H), 8.83 (d, 1H). ^{13}C NMR (125 MHz, $CDCl_3$, 298 K, TMS): δ 28.1, 55.9, 59.4, 81.1, 86.8, 95.2, 114.2, 121.7, 122.9, 124.1, 127.6, 129.5, 130.3, 131.6, 139.3, 141.9, 142.3, 145.0, 149.0, 151.6, 152.0, 157.9, 159.4, 160.3, 162.4, 163.9, 164.0, 170.4. ESI-MS: m/z 1984 [3%, $(M - PF_6)^+$], 992 [20%, $(M - PF_6 + H)^{2+}$], 662 [100%, $(M - PF_6 + 2H)^{3+}$] all with correct isotope patterns and spacings.

*Complex **E**.* The Ir(III) complex **D** (0.532 g, 0.25 mmol) was dissolved in DCM (20 cm^3) and cooled to 0 °C. An excess of cold trifluoroacetic acid (5 cm^3) was added to this cold solution dropwise while stirring under an argon atmosphere. The resulting mixture was stirred for 16 h at 0 °C, after which solvents and other volatile substances were removed *in vacuo*. The residue was triturated with ether (5 × 25 cm^3) and finally filtered to afford the product as a yellow mass, which was dried *in vacuo* overnight. The isolated yield was 0.260 g (62%). ^{1}H NMR (500 MHz, DMSO-d^6, 298 K, TMS): δ 3.48 (s, 16H), 3.95 (s, 8H), 5.68 (d, 1H), 5.72 (d, 1H), 6.98−7.09 (m, 4H), 7.28 (s, 1H), 7.51 (s, 1H), 7.59 (s, 2H), 7.70−7.73 (m, 2H), 7.97−8.00 (m, 2H), 8.28−8.31 (m, 4H), 8.43 (s, 2H), 9.29 (d, 2H), 12.42 (br s, 8H). ^{13}C NMR (125 MHz, $CDCl_3$, 298 K, TMS): δ 54.4, 58.9, 88.3, 93.3, 113.5, 121.1, 121.5, 122.4, 122.9, 123.5, 124.4, 128.0, 128.9, 129.6, 131.1, 139.9, 142.5, 144.6, 150.6, 152.8, 157.9, 159.6, 161.6, 162.6, 163.6, 172.3. ESI-MS: m/z: 1535 [25%, $(M - CF_3CO_2)^+$], 1490 [90%, $(M - CF_3CO_2 - HCOOH)]^+$

*Complexes **Ir·Ln$_2$** (Ln = Eu(III), Gd(III); Isolated as Na$^+$ salts).* To a solution of complex **E** (0.059 g, 0.035 mmol) in MeOH (5 cm^3) was added the appropriate $Ln(OTf)_3$ (0.045 g, 0.075 mmol). The mixture was stirred for 30 min, after which 1 M aqueous NaOH was added slowly to afford a pH of 5. The reaction mixture was then stirred at 50 °C for 2 days. Solvents were then evaporated, and the residue was dissolved in the minimum amount of MeOH and reprecipitated by the gradual addition of ether; this reprecipitation was repeated several times after which the product was dried *in vacuo*. Isolated yield: ca. 0.05 g (75%); the products were pure by HPLC (see the Supporting Information). Negative-ion ESI-MS for **Ir·Eu$_2$**: m/z 1831 (100%, $[M - Na]^-$). ESI-MS for **Ir·Gd$_2$**: m/z 1842 (100%, $[M - Na]^-$). These molecular ions in ESI-MS showed the correct isotope patterns and spacings.

Cell Culture and Staining. *Culture.* HeLa cells were cultured in a humidified 37 °C, 5% CO_2/95% air (v/v) environment in Modified Eagle's Medium (MEM) supplemented with 10% (v/v) fetal calf serum (FCS), 1% penicillin-streptomycin and 2 mM L-glutamine. Cells were cultured as monolayers in T-75 flasks and passaged using trypsin-EDTA. For confocal and PLIM imaging experiments, cells were seeded in to 35 mm MatTek glass-bottomed dishes until 60% confluent.

Staining. After removal of growth media, cells were washed with PBS (phosphate-buffered saline, 1 mL/well) before treating with a solution of the appropriate Ir/Ln complex: 25−100 μM in full MEM (0.04−0.4% DMSO, 16 h at 37 °C, 1 mL/well). All incubation solutions were diluted from a 20 mM stock solution of **Ir·Ln** in DMSO, with the exception of **Ir·Eu$_2$** which was diluted from a 10 mM stock. After incubation, cells were washed with PBS (3 × 1 mL/well) to remove excess complex, then imaged in 2−3 mL of Phenol Red-free MEM media.

Co-staining with Lysotracker Red. After incubating with **Ir·Ln**, cells were washed with PBS (3 × 1 mL/well) before the addition of lysotracker Red (Life Technologies), 50 nM in full MEM media for 30 min at 37 °C, after which cells were washed with PBS and covered with fresh media before imaging.

Confocal Imaging. Confocal images were recorded using an inverted Nikon Model Eclipse C2 system that was attached to a Nikon Model Ti−U system, with 405, 488, and 561 nm coupled lasers, as a combined laser-hub unit from Omicron (UK). For imaging, a Nikon 100× Apo oil immersion objective (NA 1.49) was used, along with 405 nm excitation for **Ir·Ln** and **Ir·Ln$_2$**, and 561 nm excitation for lysotracker Red. Emission filters used were 515/30 for **Ir·Ln** and 590 nm long pass (lp) filter for lysotracker red.

O_2 Dependence on Ir·Gd and Lifetime Imaging. *Sample Preparation.* Solutions of **Ir·Gd** in distilled water and full MEM media (1×10^{-4} M), diluted from a 20 mM DMSO stock, were placed in Mat Tek 35 mm glass-bottomed dishes, and the excitation light focused into the bulk of the solution. For fixed cell samples, HeLa cells were cultured to 60% confluency in Mat Tek 35 mm glass-bottomed dishes before incubation with **Ir·Gd** (50 μM, 16 h at 37 °C). After washing and fixation, cells were covered with PBS for imaging.

Gas Mixtures of O_2 and N_2. Gas mixtures of O_2 and N_2 with a flow rate of 100 mL/min were controlled using Mass View flow meters (Model MV-302, Bronkhorst). Samples were equilibrated for 20 min (at RT) with each gas mixture, using a bespoke lid (with inlet and outlet), before PLIM imaging.

Single Photon PLIM Imaging. A single-photon (405 nm) phosphorescence lifetime imaging unit was used to record emission lifetimes of **Ir·Gd** solutions at varying levels of O_2. This system comprised a Becker & Hickl BDL405 SM laser and DCS120 attached to a Nikon Ti-E inverted microscope.

Two-Photon PLIM Imaging. A multiphoton (760 nm) phosphorescence lifetime imaging unit comprised an adapted Becker & Hickl DCS120 confocal scanning system and Coherent Mira 900F laser pumped by a Verdi V10, connected to a Nikon Ti-E inverted microscope, was used to image fixed cells stained with **Ir·Gd** under varying levels of O_2.

A water immersion 60× (NA 1.2) objective was used for all samples. Emission light was collected from 485 nm to 650 nm, using appropriate filters.

PLIM Data Collection and Processing. A PLIM imaging window of 24 μs was used for all samples. Regions of interest (entire field of view for solutions, individual cells for fixed cell samples) were analyzed in SPCImage (Becker & Hickl software, version 5.0) and in Origin (version 6.0). In all cases, the data were most appropriately fitted to a double exponential decay model. Reported lifetimes and lifetime maps depict the major emission component τ_1.

■ ASSOCIATED CONTENT

Ⓢ Supporting Information

The Supporting Information is available free of charge on the ACS Publications website at DOI: 10.1021/acs.inorgchem.6b00702.

Characterization of **Ir·Ln$_2$** and precursor complexes (NMR, mass spectra, UV-vis and emission spectra, and calculated MO diagrams). MTT procedure and toxicity data for dyads (**Ir·Ln**) and triads (**Ir·Ln$_2$**). Luminescence decay traces of **Ir·Gd** at varying concentration, and from 0 to 100% O_2 in cell media and aqueous solution. Confocal imaging of **Ir·Ln$_2$** in HeLa cells, two-photon absorption cross-section (calculation and data process-

DOI: 10.1021/acs.inorgchem.6b00702
Inorg. Chem. XXXX, XXX, XXX−XXX

ing), calculation showing conversion of % O_2 to [μM] O_2; tabulated DFT data (PDF)

AUTHOR INFORMATION

Corresponding Authors

*E-mail: liz.baggaley@sheffield.ac.uk (E. Baggaley).
*E-mail: m.d.ward@sheffield.ac.uk (M. D. Ward).

Notes

The authors declare no competing financial interest.

ACKNOWLEDGMENTS

We thank the European Commission for a Marie Curie International Incoming Fellowship to A.J. The Central Laser Facility (CLF) received funding from the European Union's Horizon 2020 Research and Innovation Programme, under Grant Agreement No. 654148 Laserlab-Europe.

REFERENCES

(1) (a) Ward, M. D. *Coord. Chem. Rev.* **2007**, *251*, 1663−1677. (b) Faulkner, S.; Natrajan, L. S.; Perry, W. S.; Sykes, D. *Dalton Trans.* **2009**, 3890−3899. (c) Ward, M. D. *Coord. Chem. Rev.* **2010**, *254*, 2634−2642. (d) Chen, F.-F.; Chen, Z.-Q.; Bian, Z.-Q.; Huang, C.-H. *Coord. Chem. Rev.* **2010**, *254*, 991−1010. (e) Aboshyan-Sorgho, L.; Cantuel, M.; Petoud, S.; Hauser, A.; Piguet, C. *Coord. Chem. Rev.* **2012**, *256*, 1644−1663. (f) Xu, L.-J.; Xu, G.-T.; Chen, Z.-N. *Coord. Chem. Rev.* **2014**, *273-274*, 47−62.

(2) Flamigni, L.; Barbieri, A.; Sabatini, C.; Ventura, B.; Barigelletti, F. *Top. Curr. Chem.* **2007**, *281*, 143−203.

(3) (a) Tart, N. M.; Sykes, D.; Sazanovich, I.; Tidmarsh, I. S.; Ward, M. D. *Photochem. Photobiol. Sci.* **2010**, *9*, 886−889. (b) Sykes, D.; Tidmarsh, I. S.; Barbieri, A.; Sazanovich, I. V.; Weinstein, J. A.; Ward, M. D. *Inorg. Chem.* **2011**, *50*, 11323−11339. (c) Sykes, D.; Ward, M. D. *Chem. Commun.* **2011**, *47*, 2279−2281. (d) Sykes, D.; Parker, S. C.; Sazanovich, I. V.; Stephenson, A.; Weinstein, J. A.; Ward, M. D. *Inorg. Chem.* **2013**, *52*, 10500−10511. (e) Sykes, D.; Cankut, A. J.; Mohd Ali, N.; Stephenson, A.; Spall, S. J. P.; Parker, S. C.; Weinstein, J. A.; Ward, M. D. *Dalton Trans.* **2014**, *43*, 6414−6428. (f) Baggaley, E.; Cao, D.-K.; Sykes, D.; Botchway, S. W.; Weinstein, J. A.; Ward, M. D. *Chem.—Eur. J.* **2014**, *20*, 8898−8903.

(4) (a) Coppo, P.; Duati, M.; Kozhevnikov, V. N.; Hofstraat, J. W.; De Cola, L. *Angew. Chem., Int. Ed.* **2005**, *44*, 1806−1810. (b) Chen, F.-F.; Bian, Z.-Q.; Liu, Z.-W.; Nie, D.-B.; Chen, Z.-Q.; Huang, C.-H. *Inorg. Chem.* **2008**, *47*, 2507−2513. (c) Jiang, W.; Lou, B.; Wang, J.; Lv, H.; Bian, Z.; Huang, C. *Dalton Trans.* **2011**, *40*, 11410−11418. (d) Jones, J. E.; Jenkins, R. L.; Hicks, R. S.; Hallett, A. J.; Pope, S. J. A. *Dalton Trans.* **2012**, *41*, 10372−10381. (e) Yu, G.; Xing, Y.; Chen, F.; Han, R.; Wang, J.; Bian, Z.; Fu, L.; Liu, Z.; Ai, X.; Zhang, J.; Huang, C. *ChemPlusChem* **2013**, *78*, 852−859. (f) Chen, F.-F.; Wei, H.-B.; Bian, Z.-Q.; Liu, Z.-W.; Ma, E.; Chen, Z.-N.; Huang, C.-H. *Organometallics* **2014**, *33*, 3275−3282. (g) Li, L.; Zhang, S.; Xu, L.; Chen, Z.-N.; Luo, J. *J. Mater. Chem. C* **2014**, *2*, 1698−1703. (h) Zhao, Q.; Liu, Y.; Cao, Y.; Lv, W.; Yu, Q.; Liu, S.; Liu, X.; Shi, M.; Huang, W. *Adv. Opt. Mater.* **2015**, *3*, 233−240.

(5) (a) Bünzli, J.-C. G. *Chem. Rev.* **2010**, *110*, 2729−2755. (b) New, E. J.; Parker, D.; Smith, D. G.; Walton, J. W. *Curr. Opin. Chem. Biol.* **2010**, *14*, 238−246. (c) Zhao, Q.; Huang, C.; Li, F. *Chem. Soc. Rev.* **2011**, *40*, 2508−2524. (d) Baggaley, E.; Weinstein, J. A.; Williams, J. A. G. *Coord. Chem. Rev.* **2012**, *256*, 1762−1785. (e) Coogan, M. P.; Fernández-Moreira, V. *Chem. Commun.* **2014**, *50*, 384−399. (f) Lo, K. K.-W.; Li, S. P.-Y. *RSC Adv.* **2014**, *4*, 10560−10585.

(6) (a) Bachmann, L.; Zezell, D. M.; Ribeiro, A. D.; Gomes, L.; Ito, A. S. *Appl. Spectrosc. Rev.* **2006**, *41*, 575−590. (b) Johnsson, N.; Johnsson, K. *ACS Chem. Biol.* **2007**, *2*, 31−38. (c) Hötzer, B.; Medintz, I. L.; Hildebrandt, N. *Small* **2012**, *8*, 2297−2326.

(7) (a) Sakadžić, S.; Roussakis, E.; Yaseen, M. A.; Mandeville, E. T.; Srinivasan, V. J.; Arai, K.; Ruvinskaya, S.; Devor, A.; Lo, E. H.; Vinogradov, S. A.; Boas, D. A. *Nat. Methods* **2010**, *7*, 755−759. (b) Becker, W.; Su, B.; Bergmann, A.; Weisshart, K.; Holub, O. In *Multiphoton Microscopy in the Biomedical Sciences XI*; Proceedings of the SPIE, No. *7903*, SPIE: Bellingham, WA, 2011; pp 20−27. (c) Lecoq, J.; Parpaleix, A.; Roussakis, E.; Ducros, M.; Houssen, Y. G.; Vinogradov, S. A.; Charpak, S. *Nat. Med.* **2011**, *17*, 893−898. (d) Papkovsky, D. B.; Zhdanov, A. V.; Fercher, A.; Dmitriev, R. I.; Hynes, J. *Phosphorescent Oxygen-Sensitive Probes*; Springer Briefs in Biochemistry and Molecular Biology; Springer: Basel, Switzerland, 2012; pp 71−103. (e) Papkovsky, D. B.; Dmitriev, R. I. *Chem. Soc. Rev.* **2013**, *42*, 8700−8732. (f) Kazmi, S. M. S.; Salvaggio, A. J.; Estrada, A. D.; Hemati, M. A.; Shaydyuk, N. K.; Roussakis, E.; Jones, T. A.; Vinogradov, S. A.; Dunn, A. K. *Biomed. Opt. Express* **2013**, *4*, 1061−1073. (g) Baggaley, E.; Botchway, S. W.; Haycock, J. W.; Morris, H.; Sazanovich, I. V.; Williams, J. A. G.; Weinstein, J. A. *Chem. Sci.* **2014**, *5*, 879−886. (h) Baggaley, E.; Gill, M. R.; Green, N. H.; Turton, D.; Sazanovich, I. V.; Botchway, S. W.; Smythe, C.; Haycock, J. W.; Weinstein, J. A.; Thomas, J. A. *Angew. Chem., Int. Ed.* **2014**, *53*, 3367−3371. (i) Baggaley, E.; Weinstein, J. A.; Williams, J. A. G. Time-Resolved Emission Imaging Microscopy Using Phosphorescent Metal Complexes: Taking FLIM and PLIM to New Lengths. In *Luminescent and Photoactive Transition Metal Complexes as Biomolecular Probes and Cellular Reagents*; Lo, K.K.-W., Ed.; Structure and Bonding, Vol. *165*; Springer: Berlin, Heidelberg, 2014; pp 205−256.

(8) (a) Zhang, S.; Hosaka, M.; Yoshihara, T.; Negishi, K.; Iida, Y.; Tobita, S.; Takeuchi, T. *Cancer Res.* **2010**, *70*, 4490−4498. (b) Esipova, T. V.; Karagodov, A.; Miller, J.; Wilson, D. F.; Busch, T. M.; Vinogradov, S. A. *Anal. Chem.* **2011**, *83*, 8756−8765. (c) Spencer, J. A.; Ferraro, F.; Roussakis, E.; Klein, A.; Wu, J.; Runnels, J. M.; Zaher, W.; Mortensen, L. J.; Alt, C.; Turcotte, R.; Yusuf, R.; Côté, D.; Vinogradov, S. A.; Scadden, D. T.; Lin, C. P. *Nature* **2014**, *508*, 269−273. (d) Jenkins, J.; Dmitriev, R. I.; Morten, K.; McDermott, K. W.; Papkovsky, D. B. *Acta Biomater.* **2015**, *16*, 126−135. (e) Kurokawa, H.; Ito, H.; Inoue, M.; Tabata, K.; Sato, Y.; Yamagata, K.; Kizaka-Kondoh, S.; Kadonosono, T.; Yano, S.; Inoue, M.; Kamachi, T. *Sci. Rep.* **2015**, *5*, 10657.

(9) (a) Harris, A. L. *Nat. Rev. Cancer* **2002**, *2*, 38−47. (b) Murdoch, C.; Muthana, M.; Lewis, C. E. *J. Immunol.* **2005**, *175*, 6257−6263. (c) Sun, X.; He, G.; Qing, H.; Zhou, W.; Dobie, F.; Cai, F.; Staufenbiel, M.; Huang, L. E.; Song, W. *Proc. Natl. Acad. Sci. U. S. A.* **2006**, *103*, 18727−18732. (d) Simon, M. C. *Cell Metab.* **2006**, *3*, 150−151. (e) Papandreou, I.; Cairns, R. A.; Fontana, L.; Lim, A. L.; Denko, N. C. *Cell Metab.* **2006**, *3*, 187−197. (f) Taylor, C. T. *Biochem. J.* **2008**, *409*, 19−26. (g) Bertout, J. A.; Patel, S. A.; Simon, M. C. *Nat. Rev. Cancer* **2008**, *8*, 967−975.

(10) (a) Finikova, O. S.; Lebedev, A. Y.; Aprelev, A.; Troxler, T.; Gao, F.; Garnacho, C.; Muro, S.; Hochstrasser, R. M.; Vinogradov, S. A. *ChemPhysChem* **2008**, *9*, 1673−1679. (b) Dmitriev, R. I.; Zhdanov, A. V.; Ponomarev, G. V.; Yashunski, D. V.; Papkovsky, D. B. *Anal. Biochem.* **2010**, *398*, 24−33. (c) Dmitriev, R. I.; Zhdanov, A. V.; Jasionek, G.; Papkovsky, D. B. *Anal. Chem.* **2012**, *84*, 2930−2938. (d) Dmitriev, R. I.; Zhdanov, A. V.; Nolan, Y. M.; Papkovsky, D. B. *Biomaterials* **2013**, *34*, 9307−9317. (e) Tsytsarev, V.; Arakawa, H.; Borisov, S.; Pumbo, E.; Erzurumlu, R. S.; Papkovsky, D. B. *J. Neurosci. Methods* **2013**, *216*, 146−151. (f) Kelly, C. A.; Toncelli, C.; Kerry, J. P.; Papkovsky, D. B. *Sens. Actuators, B* **2014**, *203*, 935−940.

(11) (a) Wilson, D. F.; Vinogradov, S. A.; Grosul, P.; Vaccarezza, M. N.; Kuroki, A.; Bennett, J. *Appl. Opt.* **2005**, *44*, 5239−5248. (b) Lemon, C. M.; Karnas, E.; Bawendi, M. G.; Nocera, D. G. *Inorg. Chem.* **2013**, *52*, 10394−10406.

(12) (a) Sud, D.; Mehta, G.; Mehta, K.; Linderman, J.; Takayama, S.; Mycek, M.-A. *J. Biomed. Opt.* **2006**, *11*, 050504. (b) Sud, D.; Mycek, M.-A. *J. Biomed. Opt.* **2009**, *14*, 020506. (c) Choi, N. W.; Verbridge, S. S.; Williams, R. M.; Chen, J.; Kim, J.-Y.; Schmehl, R.; Farnum, C. E.; Zipfel, W. R.; Fischbach, C.; Stroock, A. D. *Biomaterials* **2012**, *33*, 2710−2722. (d) Howard, S. S.; Straub, A.; Horton, N. G.; Kobat, D.; Xu, C. *Nat. Photonics* **2012**, *7*, 33−37. (e) Khan, A. A.; Fullerton-Shirey, S. K.; Howard, S. S. *RSC Adv.* **2015**, *5*, 291−300. (f) Zhang, P.;

DOI: 10.1021/acs.inorgchem.6b00702
Inorg. Chem. XXXX, XXX, XXX−XXX

Huang, H.; Chen, Y.; Wang, J.; Ji, L.; Chao, H. *Biomaterials* **2015**, *53*, 522−531.
(13) (a) Yoshihara, T.; Yamaguchi, Y.; Hosaka, M.; Takeuchi, T.; Tobita, S. *Angew. Chem., Int. Ed.* **2012**, *51*, 4148−4151. (b) Lv, W.; Yang, T.; Yu, Q.; Zhao, Q.; Zhang, K. Y.; Liang, H.; Liu, S.; Li, F.; Huang, W. *Adv. Sci.* **2015**, *2*, 1500107. (c) Zheng, X.; Tang, H.; Xie, C.; Zhang, J.; Wu, W.; Jiang, X. *Angew. Chem., Int. Ed.* **2015**, *54*, 8094−8099. (d) Yoshihara, T.; Murayama, S.; Masuda, T.; Kikuchi, T.; Yoshida, K.; Hosaka, M.; Tobita, S. *J. Photochem. Photobiol., A* **2015**, *299*, 172−182. (e) Zheng, X.; Wang, X.; Mao, H.; Wu, W.; Liu, B.; Jiang, X. *Nat. Commun.* **2015**, *6*, 5834.
(14) Jana, A.; Baggaley, E.; Amoroso, A.; Ward, M. D. *Chem. Commun.* **2015**, *51*, 8833−8836.
(15) Lazarides, T.; Sykes, D.; Faulkner, S.; Barbieri, A.; Ward, M. D. *Chem.—Eur. J.* **2008**, *14*, 9389−9399.
(16) (a) Costa, J.; Ruloff, R.; Burai, L.; Helm, L.; Merbach, A. E. *J. Am. Chem. Soc.* **2005**, *127*, 5147−5157. (b) Werner, E. J.; Datta, A.; Jocher, C. J.; Raymond, K. N. *Angew. Chem., Int. Ed.* **2008**, *47*, 8568−8580. (c) Datta, A.; Raymond, K. N. *Acc. Chem. Res.* **2009**, *42*, 938−947 and references therein.10.1021/ar800250h (d) Garimella, P. D.; Datta, A.; Romanini, D. W.; Raymond, K. N.; Francis, M. B. *J. Am. Chem. Soc.* **2011**, *133*, 14704−14709. (e) Stasiuk, G. J.; Smith, H.; Wylezinska-Arridge, M.; Tremoleda, J. L.; Trigg, W.; Luthra, S. K.; Iveson, V. M.; Gavins, F. N. E.; Long, N. J. *Chem. Commun.* **2013**, *49*, 564−566. (f) Sour, A.; Jenni, S.; Ortí-Suárez, A.; Schmitt, J.; Heitz, V.; Bolze, F.; Loureiro de Sousa, P.; Po, C.; Bonnet, C. S.; Pallier, A.; Tóth, E.; Ventura, B. *Inorg. Chem.* **2016**, *55*, 4545−4554.
(17) (a) Koullourou, T.; Natrajan, L. S.; Bhavsar, H.; Pope, S. J. A.; Feng, J. H.; Narvainen, J.; Shaw, R.; Scales, E.; Kauppinen, R.; Kenwright, A. M.; Faulkner, S. *J. Am. Chem. Soc.* **2008**, *130*, 2178−2179. (b) Verwilst, P.; Eliseeva, S. V.; Vander Elst, L.; Burtea, C.; Laurent, S.; Petoud, S.; Muller, R. N.; Parac-Vogt, T. N.; De Borggraeve, W. M. *Inorg. Chem.* **2012**, *51*, 6405−6411. (c) Tropiano, M.; Record, C. J.; Morris, E.; Rai, H. S.; Allain, C.; Faulkner, S. *Organometallics* **2012**, *31*, 5673−5676. (d) Luo, J.; Li, W.-S.; Xu, P.; Zhang, L.-Y.; Chen, Z.-N. *Inorg. Chem.* **2012**, *51*, 9508−9516. (e) Zhang, X.; Jing, X.; Liu, T.; Han, G.; Li, H.; Duan, C. *Inorg. Chem.* **2012**, *51*, 2325−2331. (f) Rivas, C.; Stasiuk, G. J.; Gallo, J.; Minuzzi, F.; Rutter, G. A.; Long, N. J. *Inorg. Chem.* **2013**, *52*, 14284−14293. (g) Luo, J.; Chen, L.-F.; Hu, P.; Chen, Z.-N. *Inorg. Chem.* **2014**, *53*, 4184−4191. (h) Stasiuk, G. J.; Minuzzi, F.; Sae-Heng, M.; Rivas, C.; Juretschke, H.-S; Piemonti, L.; Allegrini, P. R.; Laurent, D.; Duckworth, A. R.; Beeby, A.; Rutter, G. A.; Long, N. J. *Chem.—Eur. J.* **2015**, *21*, 5023−5033.
(18) (a) Tóth, E.; Helm, L.; Merbach, A. E. *Comprehensive Coordination Chemistry II*, Vol. *9*; McCleverty, J. A., Meyer, T. J., Eds.; Elsevier: Oxford, U.K., 2004; Chapter 9.19, pp 841−881. (b) Kowalewski, J.; Nordenskiöld, L.; Benetis, N.; Westlund, P.-O. *Prog. Nucl. Magn. Reson. Spectrosc.* **1985**, *17*, 141−185. (c) Solomon, I. *Phys. Rev.* **1955**, *99*, 559−565. (d) Bloembergen, N. *J. Chem. Phys.* **1957**, *27*, 572−573. (e) Bloembergen, N.; Morgan, L. O. *J. Chem. Phys.* **1961**, *34*, 842−850.
(19) (a) Sato, S.; Wada, M. *Bull. Chem. Soc. Jpn.* **1970**, *43*, 1955−1962. (b) Parker, D. *Coord. Chem. Rev.* **2000**, *205*, 109−130.
(20) Williams, J. A. G.; Beeby, A.; Davies, E. S.; Weinstein, J. A.; Wilson, C. *Inorg. Chem.* **2003**, *42*, 8609−8611.
(21) Frisch, M. J.; Trucks, G. W.; Schlegel, H. B.; Scuseria, G. E.; Robb, M. A.; Cheeseman, J. R.; Scalmani, G.; Barone, V.; Mennucci, B.; Petersson, G. A.; Nakatsuji, H.; Caricato, M.; Li, X.; Hratchian, H. P.; Izmaylov, A. F.; Bloino, J.; Zheng, G.; Sonnenberg, J. L.; Hada, M.; Ehara, M.; Toyota, K.; Fukuda, R.; Hasegawa, J.; Ishida, M.; Nakajima, T.; Honda, Y.; Kitao, O.; Nakai, H.; Vreven, T.; Montgomery, J. A., Jr.; Peralta, J. E.; Ogliaro, F.; Bearpark, M.; Heyd, J. J.; Brothers, E.; Kudin, K. N.; Staroverov, V. N.; Kobayashi, R.; Normand, J.; Raghavachari, K.; Rendell, A.; Burant, J. C.; Iyengar, S. S.; Tomasi, J.; Cossi, M.; Rega, N.; Millam, N. J.; Klene, M.; Knox, J. E.; Cross, J. B.; Bakken, V.; Adamo, C.; Jaramillo, J.; Gomperts, R.; Stratmann, R. E.; Yazyev, O.; Austin, A. J.; Cammi, R.; Pomelli, C.; Ochterski, J. W.; Martin, R. L.; Morokuma, K.; Zakrzewski, V. G.; Voth, G. A.; Salvador, P.; Dannenberg, J. J.; Dapprich, S.; Daniels, A. D.; Farkas, Ö.; Foresman, J. B.; Ortiz, J. V.; Cioslowski, J.; Fox, D. J. *Gaussian 09, Revision A.1*; Gaussian, Inc.: Wallingford, CT, 2009.
(22) (a) Lee, C.; Yang, W.; Parr, R. G. *Phys. Rev. B: Condens. Matter Mater. Phys.* **1988**, *37*, 785−789. (b) Becke, A. D. *J. Chem. Phys.* **1993**, *98*, 5648−5652. (c) Rubio-Pons, O.; Luo, Y.; Ågren, H. *J. Chem. Phys.* **2006**, *124*, 094310-1−094310-5.
(23) (a) Hay, P. J.; Wadt, W. R. *J. Chem. Phys.* **1985**, *82*, 270−283. (b) Wadt, W. R.; Hay, P. J. *J. Chem. Phys.* **1985**, *82*, 284−298. (c) Hay, P. J.; Wadt, W. R. *J. Chem. Phys.* **1985**, *82*, 299−310.
(24) Han, G.; Deng, Y.; Sun, J.; Ling, J.; Shen, Z. *Exp. Ther. Med.* **2015**, *9*, 1561−1566.
(25) (a) Caillé, F.; Bonnet, C. S.; Buron, F.; Villette, S.; Helm, L.; Petoud, S.; Suzenet, F.; Tóth, E. *Inorg. Chem.* **2012**, *51*, 2522−2532. (b) Pellegatti, L.; Zhang, J.; Drahos, B.; Villette, S.; Suzenet, F.; Guillaumet, G.; Petoud, S.; Tóth, E. *Chem. Commun.* **2008**, 6591−6593.
(26) Comblin, V.; Gilsoul, D.; Hermann, M.; Humblet, V.; Jacques, V.; Mesbahi, M.; Sauvage, C.; Desreux, J. F. *Coord. Chem. Rev.* **1999**, *185−186*, 451−470.
(27) Dunn, K. W.; Kamocka, M. M.; McDonald, J. H. *Am. J. Physiol. Cell Physiol.* **2011**, *300*, C723−C742.
(28) (a) Fernandez-Moreira, V.; Thorp-Greenwood, F. L.; Amoroso, A. J.; Cable, J.; Court, J. B.; Gray, V.; Hayes, A. J.; Jenkins, R. L.; Kariuki, B. M.; Lloyd, D.; Millet, C. O.; Williams, C. F.; Coogan, M. P. *Org. Biomol. Chem.* **2010**, *8*, 3888−3901. (b) Zhang, K. Y.; Liu, H.-W.; Fong, T. T.-H.; Chen, X.-G.; Lo, K. K.-W. *Inorg. Chem.* **2010**, *49*, 5432−5443.
(29) Wragg, A.; Gill, M. R.; McKenzie, L.; Glover, C.; Mowll, R.; Weinstein, J. A.; Su, X.; Smythe, C.; Thomas, J. A. *Chem.—Eur. J.* **2015**, *21*, 11865−11871.
(30) Tiede, L. M.; Cook, E. A.; Morsey, B.; Fox, H. S. *Cell Death Dis.* **2011**, *2*, 246.

DOI: 10.1021/acs.inorgchem.6b00702
Inorg. Chem. XXXX, XXX, XXX−XXX